CHALMERS
UNIVERSITY OF TECHNOLOGY

Adaptive Determination of Optimum Switching Frequency in SiC-PWM-based Motor Drives: A Speed-Dependent Core Loss Correction

Citation for the original published paper (version of record):
Amirpour, S., Soltanipour, S., Thiringer, T. et al (2025). Adaptive Determination of Optimum Switching Frequency in SiC-PWM-based Motor Drives: A Speed-Dependent Core Loss Correction Approach. IEEE Open Journal of the Industrial Electronics Society, 6: 883-897. http://dx.doi.org/10.1109/OJIES.2025.3569349

(article starts on next page)

IEEE Open Journal of the
Industrial Electronics Society

Received 20 February 2025; accepted 5 May 2025. Date of publication 12 May 2025;
date of current version 2 June 2025. The review of this article was arranged by Associate Editor Ritesh Kumar Keshri.

Digital Object Identifier 10.1109/OJIES.2025.3569349

Adaptive Determination of Optimum Switching Frequency in SiC-PWM-Based Motor Drives: A Speed-Dependent Core Loss Correction Approach

SEPIDEH AMIRPOUR [1], SIMA SOLTANIPOUR [2] (Member, IEEE), TORBJÖRN THIRINGER [3] (Senior Member, IEEE), AND PRANAV KATTA [2]

[1]ZEEKR Technology Europe, SE-41755 Gothenburg, Sweden
[2]Volvo Cars Corporations, SE-40531 Gothenburg, Sweden
[3]Chalmers University of Technology, Gothenburg, SE-41296, Sweden

CORRESPONDING AUTHOR: SEPIDEH AMIRPOUR (e-mail: sepideh.amirpour@zeekrtech.eu).

This work was supported by the ZEEKR Technology Europe and Volvo Cars and Energimyndigheten.

ABSTRACT This study focuses on identifying the optimal switching frequency for silicon-carbide (SiC)-based motor drives across a wide range of operating conditions using a loss minimization strategy. The results are then compared with those of traditional silicon-insulated-gate bipolar transistor (IGBT) systems. The approach involves conducting a comprehensive real-time finite element method (FEM) analysis of losses induced by pulsewidth modulation (PWM) voltages in an interior permanent magnet synchronous machine, compared to conventional sinusoidal current excitation feeding. The analysis integrates electromagnetic field simulations in Ansys Maxwell with the drive system control algorithm in Ansys Twin Builder, ensuring an accurate representation of their interactions. In addition, a method utilizing speed-adaptive core loss coefficients, which account for variable frequencies, is implemented for a more precise core loss estimation. The results reveal a notable discrepancy of up to 80% in the core loss calculations when using speed-adaptive coefficients versus fixed coefficients. By employing the real-time coupled simulations, the higher switching capabilities of SiC MOSFETs could be effectively realized to optimize the PWM frequency over a broader range (10–50 kHz), particularly in the main drive region of electric vehicles, with differences of up to 20 kHz compared to IGBT systems. Furthermore, applying the proposed optimal PWM frequency profile in the worldwide harmonized light vehicle test cycle leads to a reduction of up to 22% in accumulated energy losses in the SiC motor drive compared to its IGBT counterpart.

INDEX TERMS Core losses, electrified vehicles, energy efficiency, silicon-carbide (SiC)-based motor drives, voltage-source inverters (VSI), variable switching frequency, permanent magnet synchronous machine, pulsewidth modulation (PWM)-induced power losses.

I. INTRODUCTION

As global demand for electric vehicles (EVs) continues to rise, improving the efficiency of propulsion motor drive systems becomes increasingly imperative. Compared to widely used silicon insulated-gate bipolar transistor (Si-IGBT), wide-bandgap (WBG) technologies—gallium-nitride (GaN) and silicon-carbide (SiC) switching devices—have recently gained prominence in modern electric powertrains due to their faster switching transitions, lower ON-state and switching losses and ability to operate at higher switching frequencies [1], [2], [3]. These features are particularly beneficial in permanent magnet synchronous motors (PMSMs) and three-phase voltage source inverters (VSI), as increasing the switching frequency reduces the harmonic content in the motor's three-phase current waveforms, leading to lower motor losses by minimizing current ripples. However, setting the

switching frequency too high leads to a proportional increase in inverter losses. Hence, it is crucial to obtain an optimized switching frequency for maximizing the overall efficiency of motor drive systems. Several studies have examined variable switching frequency pulsewidth modulation (VSFPWM), where the carrier frequency of the pulsewidth modulation (PWM) is adjusted based on prediction models to control current ripple and reduce inverter switching losses. Methods like those in [4], [5], and [6] reduce switching loss in a three-phase VSI. These methods introduce optimizations that maintain output current quality similar to space vector pulsewidth modulation (SVPWM). However, they do not include detailed machine loss analyses, particularly for motor drive systems in EVs, where speed and torque vary adaptively. [7] introduces a VSFPWM method based on achieving a desired current ripple for a SiC-based PMSM drive system, taking into account a wide range of machine speeds and torques. However, the optimum switching frequency for each rotor speed and electrical torque is calculated leveraging analytical PMSM models and manufacturer-supplied loss models without utilizing finite element method (FEM)-based loss maps for greater accuracy. In addition, the analysis likely uses fixed iron loss coefficients for the iron loss calculation.

Moreover, studies, such as [8], provide valuable comparisons of motor drive losses and the effect of switching frequency in SiC MOSFETs versus Si-IGBTs, demonstrating 60%–90% iron loss reduction at high switching frequency for some selected operating points, while Nakayama et al. [9] investigated the impact of increasing switching frequency on system losses in a small GaN drive system. A limitation in these studies is that they did not quantify the results on a drive cycle level. A similar approach, which however utilizes the worldwide harmonized light vehicle test cycle (WLTC) mode driving is given in [10]. Although, the above studies reveal that operating at higher switching frequencies can yield higher total drive efficiency, attributed to the tradeoff between motor and converter losses; unfortunately, the loss models used to determine the optimum switching frequency lack a comprehensive basis utilizing FEM analyses and detailed inverter and machine loss modeling. [11] provides a FEM analysis of PWM power losses in an interior permanent magnet (IPM) machine, excited by a WBG-based inverter and, a dynamic Jiles–Atherton (J-A) model, as proposed in [12] is used to estimate PWM-induced core losses. Despite the detailed loss analysis, the study is limited to a few sets of operating conditions and the frequency dependence of core losses on operating conditions is not investigated. Furthermore, on the system level, an optimized switching frequency profile covering the entire torque-speed range or a drive cycle pattern is not fully explored. In addition, the J-A model typically requires extensive measurements and material data for the electrical steel sheets, which are not always provided by manufacturers. In [13], the study suggests an improved method of calculating core losses by using frequency adaptive hysteresis loss coefficients, while the excess and classical eddy current loss coefficients vary according to flux density levels. However, measurements and analysis are limited to a maximum frequency of 400 Hz, which leaves their impact on traction applications with wider speed and torque ranges unexplored.

To summarize, to the best of the authors' knowledge, existing methods in the literature for optimizing switching frequency, particularly for the SiC motor drive regions, either based on current ripple prediction or based on loss maps of the drive system, remain limited in their application to EVs. In this context, this study aims to address these gaps by generating full powertrain loss maps as the key metric for reliably determining the optimal switching frequency across all drive regions. The main contributions of this work are as follows.

1) *Improved Core Loss Prediction Through FEM Analysis:* The method utilizes measurements on electro-steel sheets across a broad range of frequencies and flux levels for the used iron material, calculates core loss coefficients that are dynamically updated based on the specific supply frequencies at each operating point, as well as incorporates the effect of PWM on the core loss calculation. Unlike traditional FEM tools, which use a single set of eddy and hysteresis loss coefficients for all frequencies, this method provides more reasonable core loss predictions.
2) *Comprehensive Coupled Time-Stepping FEM Analysis:* The work integrates both PMSM and inverter losses in real-time simulation, captures their interaction with varying PWM switching frequencies, predicts the corresponding current ripple characteristics, and provides more accurate inputs for the inverter loss modeling. The analysis accounts for e-machine space harmonics, PWM-induced harmonics as well as current controller interactions, closely mimicking a real-world implementation. This real-time coupled FEM simulation approach, is not thoroughly covered in the existing literature reviewed by the authors.

Finally, an additional contribution is quantifying the impact of the generated optimum PWM frequency profile on the WLTC driving pattern, analyzing drive system energy losses for the SiC system, and comparing the results with the IGBT-based counterpart.

To sum up, the main novelty of this work lies in its real-time coupled PWM-based FEM analysis that integrates both motor and inverter losses, replicating real-world operation, and facilitating the optimization of the switching frequency while dynamically improving core loss predictions for enhanced EV efficiency. Hence, this work bridges the gaps between research, development, and implementation, driving the future of more efficient EVs, and serving as a solution to accelerate the transition to sustainable energy.

II. ELECTRIC DRIVE SYSTEM

As previously mentioned, the baseline electric drive system, comprising a SiC-based inverter and a PMSM machine depicted in Fig. 1, has been configured within a real-time cosimulation between Twin Builder and Ansys Maxwell with

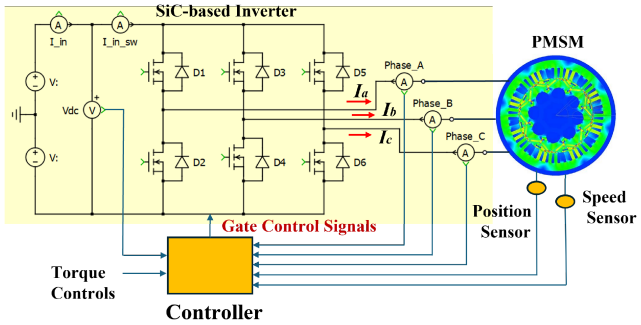

FIGURE 1. Baseline configuration of SiC-based electric drive system.

variable time-steps less than 100 ns to comprehensively capture their interaction. Furthermore, Fig. 2 illustrates the overall PMSM field-oriented control (FOC) block diagram of the drive system, showing current control loops on the dq-axis implemented in Twin Builder, as well as the maximum torque per ampere and maximum torque per volt strategies.

By applying speed-adaptive corrected core loss coefficients, key input data—such as machine reference currents, rotating speed, and dynamic inductances—are generated and fed into the FOC loop to produce the required reference voltages for the SVPWM switching pattern of the SiC VSI. The resulting three-phase PWM currents and PWM-induced voltages excite the PMSM, generating PWM-induced losses in the machine. By evaluating the total losses of the PWM-induced system (inverter and machine losses) and repeating this process throughout the operating domain with the various PWM switching frequencies within a loss minimization framework, the optimal PWM switching profile can be determined.

This design topology serves as the foundation for subsequent adjustments of the switching frequency across the entire drive region, as detailed in later sections.

A. ELECTRIC MACHINE (EM)

IPM motors are commonly used in electric and hybrid vehicles, despite concerns about the environmental impact of rare-Earth magnets. The advantage of using rare-Earth magnets lies in their ability to reduce the amount of copper and iron needed, which in turn minimizes winding and core losses. Moreover, accurate loss prediction during the design phase of EMS is critical to achieving the required efficiency and performance. However, as noted in [14], the core loss estimations from analytical models often show discrepancies of up to 100% when compared to experimental measurements of EMs. Although these discrepancies have been studied for decades, no practical usable solution has emerged, much due to the complexity of the problem.

Previous studies [13], [14], [15], [16], [17] have identified several factors contributing to the gap between core loss estimations and actual EM performance, including, the following.

1) The impact of manufacturing processes on the electrical steel laminates used in stators and rotors.
2) Harmonic content induced by the inverter switching that affects the core losses.
3) Difficulties in segregating core loss from overall machine loss obtained from measurement data.
4) Measurement inaccuracies of electrical steel properties due to measurement equipment.
5) The precision of loss models and their integration into finite element analysis (FEM) tools.

This study aims to improve core loss predictions by using FEM tools and measurements over a broad range of frequencies and flux levels for the iron materials used. Core loss coefficients are then adapted based on the machine's operating speeds.

1) SPEED-DEPENDANT CORE LOSS CALCULATION

The stator and rotor cores of the IPM under study are manufactured from silicon–iron steel laminates. The electromagnetic properties of these steel sheets are measured using standard methods, such as the Epstein Frame, as defined in IEC-60404 [18]. The key parameters for evaluating the performance of the EM, such as permeability (μ_r) and specific power loss (P_s), are measured at peak flux density (B_{pk}). The test setup is depicted in Fig. 3. The results show that as frequency increases, permeability decreases and specific core losses increase, Figs. 4 and 5. These properties are measured under sinusoidal excitation in a large number of frequency steps. In this way, a better representation can be made to determine the fundamental frequency iron loss for speed ranges across the wide operating region of a vehicle traction machine.

Iron loss models like the Bertotti model are widely used in FEM tools to predict the iron loss dependency on flux density and frequency. The dynamic Berttoti loss model is expressed by the following:

$$P_{Fe}(t) = P_h(t) + P_c(t) + P_{ex}(t) \tag{1}$$

$$P_h(t) = \left\{ \left| H_x \frac{dB_x}{dt} \right|^{2/\beta} + \left| H_y \frac{dB_y}{dt} \right|^{2/\beta} \right\}^{\beta/2} \tag{2}$$

$$P_{ec}(t) = \frac{K_{ec}}{2\pi^2} \left\{ \left(\frac{dB_x}{dt} \right)^2 + \left(\frac{dB_y}{dt} \right)^2 \right\} \tag{3}$$

$$P_{ex}(t) = \frac{K_{ex}}{C_e} \left\{ \left(\frac{dB_x}{dt} \right)^2 + \left(\frac{dB_y}{dt} \right)^2 \right\}^{0.75}. \tag{4}$$

The dynamic Bertotti loss model includes hysteresis loss coefficients k_h, classical eddy current loss coefficients k_{ec}, and excess loss coefficients k_{ex}. For silicon–iron alloys, β, a key parameter in the model, typically ranges from 1.6 to 2.2. B_x and B_y are the flux densities vectors in the x and y directions, H_x, H_y are the magnetic field strength vectors in the x and y directions. C_e is a constant value equal to 8.76. The derivation of the equations and constant values in this dynamic model is described in depth in [19]. Furthermore, k_c can be calculated by

$$k_{ec} = \pi^2 \sigma w^2 / 6 \tag{5}$$

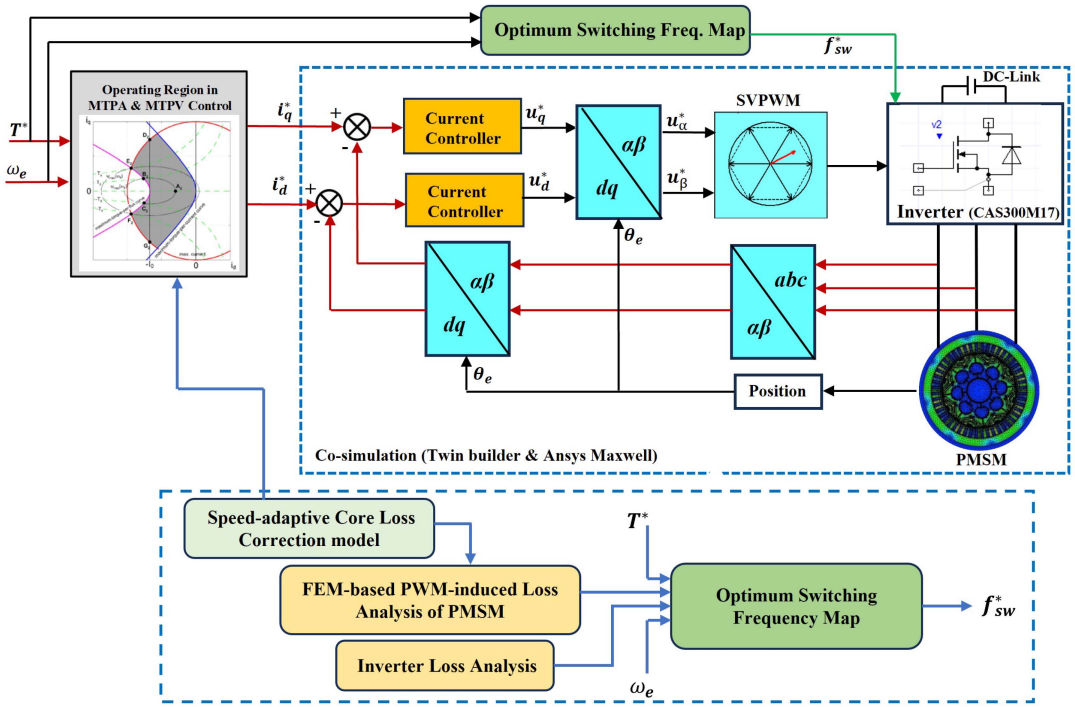

FIGURE 2. Motor drive system control block diagram.

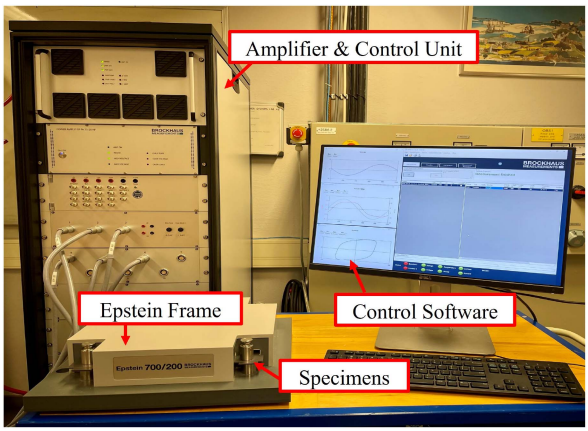

FIGURE 3. Test Setup for measuring the electrical–steel's properties.

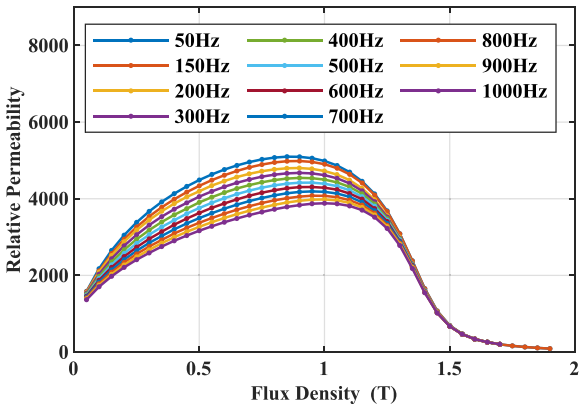

FIGURE 4. Relative permeability of the material under sinusoidal excitation with different frequencies.

where σ is conductivity and w is the thickness of the electrical steel laminates. Although including excess loss coefficients can improve curve fitting to measurement data, in this study, setting k_{ex} to zero provided better alignment, implying that classical and excess eddy current losses are treated as a combined loss component.

2) IMPLEMENTATION IN THE EM

The studied IPM machine features 48 stator slots and 8 rotor poles with double-layer V-shaped magnets. Other properties and output parameters of this EM are shown in Table 1. Fig. 6 depicts the geometry of the EM.

TABLE 1. Key parameters of the baseline EM

Parameter	Quantity	Unit
Stator outer diameter	250	mm
Rotor outer diameter	168	mm
Air gap length	1.1	mm
Active Length	119	mm
Peak power	220	kW
Peak current	250	A-RMS
Peak torque	426	Nm
DC-link voltage	800	V

Conventionally, to characterize an EM in FEM tools, a simulation is run with current excitation at a single speed value. Later these results are extrapolated for other speed ranges to

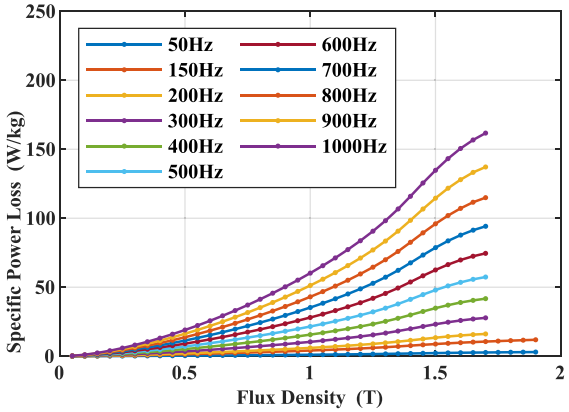

FIGURE 5. Specific power loss of the material under sinusoidal excitation with different frequencies.

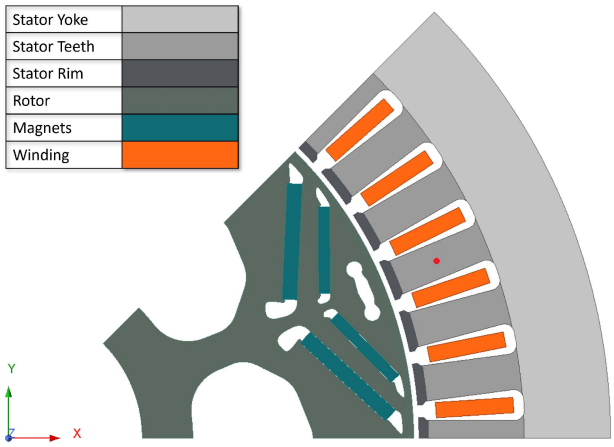

FIGURE 6. Permanent magnet synchronous machine geometry. Orange: winding, green: magnets, and gray: stator and rotor steel cores, selected point in the tooth to do further analysis on flux density is marked with red.

determine the whole machine's performance characteristics in the torque–speed map. In this method, several loss curve data obtained from measurements at different frequencies are put into the FEM tool. Then, the tool outputs a single eddy and hysteresis loss coefficient that is generated by using curve fitting of measurement data in the Berttoti model by the use of least root-mean-square error for all frequencies. Such a derivation of loss coefficients is sensitive to the choice of input frequencies and can lead to deviations from the measured data under different frequencies. To propose a more accurate use of input data, one can create a hysteresis coefficient that is frequency-dependent. In the current study, by investigating the distribution of the flux density over the cross-section of the stator core, and investigating the frequency spectrum of each element on the stator geometry, it can be seen that each part of the stator is experiencing a space harmonic content, which is for interaction between the stator slots and the shape of the magnets in the rotor. Moreover, the space harmonics of the flux density can change based on the operating point.

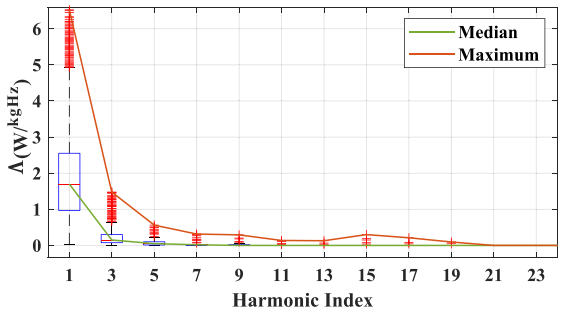

FIGURE 7. Distribution of Λ for each mesh element over the stator core at operating points throughout the speed–torque map of the IPM.

This is due to that the current angle can affect the magnetic flux that is generated from the interaction of the electromagnetic flux of the winding and the magnetic flux produced by the magnets. Hence, to evaluate the importance of including these harmonics in the accurate calculation of core losses in the Berttoti model, the flux density distribution across the frequency spectrum is analyzed. This is done for all stator elements at 248 operating points in the torque–speed map of the IPM under study.

To simplify the study and evaluate the impact of each frequency on the core loss of the machine, the parameter Λ is introduced over a mesh element,

$$\Lambda = B_{pk,n}^2 \frac{f_n}{f_1} = \frac{P_h}{f_1 K_h} \tag{6}$$

where f_n is the space harmonic frequency, f_1 is the fundamental frequency at the operating point. This parameter shows the value of hysteresis loss for each element divided by the hysteresis coefficient. Fig. 7 shows the distribution of Λ for the EM under study.

As can be seen, the median of Λ at the fundamental frequency, 1.7 $\frac{\text{W}}{\text{kgHz}}$, is more than 11 times the third space harmonic content. Another observation is that 50% of the data are in the range of 0.9–2.55 $\frac{\text{W}}{\text{kgHz}}$ in contrast to the third harmonic content, which is in the range of 0.075–0.3 $\frac{\text{W}}{\text{kgHz}}$. For the higher harmonic orders, the ratio between the median of the fundamental and the fifth-order harmonic is 34. According to this observation, it is safe to assume that the biggest portion of the core losses are generated by the flux densities appearing at the fundamental frequency. To account for the dependency of the hysteresis loss coefficient, the EM is characterized once again by simulation at each frequency level with the frequency-adaptive hysteresis loss coefficient replacing the conventional fixed coefficient. The proposed frequency-adaptive coefficient method provides a more accurate estimation of losses by prioritizing the precise calculation of the fundamental frequency, which accounts for the majority of the iron losses at a given operating point. In contrast, the conventional method consistently focuses on minimizing errors at high frequencies, potentially neglecting accuracy at lower and medium frequencies.

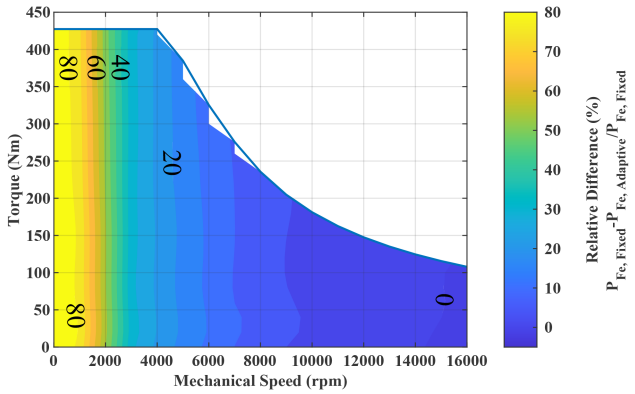

FIGURE 8. EM's core loss difference between core losses calculated from fixed and frequency-adaptive hysteresis loss coefficients.

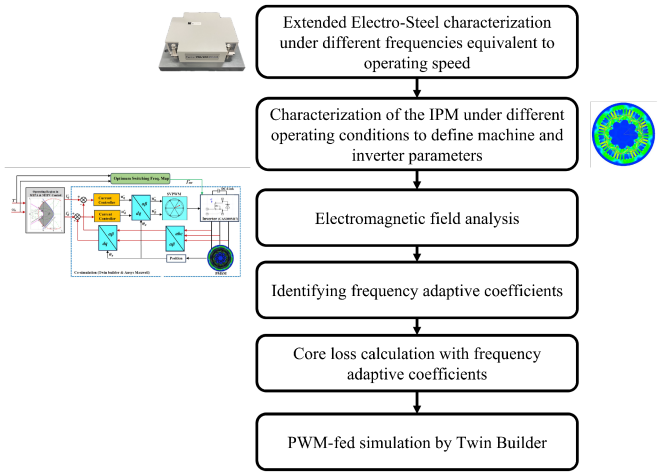

FIGURE 9. Simulation steps regarding the method to improve core loss calculation.

The iron loss results obtained from the machine's characterization using these two methods are compared. Fig. 8 illustrates the relative difference in iron losses calculated using a fixed hysteresis loss coefficient versus a frequency-adaptive hysteresis loss coefficient across the torque-speed map of the EM. As can be seen, the iron loss calculated with the fixed hysteresis loss coefficient is generally higher than that obtained with the frequency-adaptive method, except at a frequency of 1100 Hz, which corresponds to the speed region of 16 000 r/min, where it is lower by 2%. At low frequencies, the fixed coefficient method overestimates core losses by as much as 80%.

It is important to note that for the material studied, the deviation is linear since the hysteresis coefficient is the only loss coefficient assumed to be frequency-dependent. To further investigate the impact of using a frequency-adaptive coefficient on iron loss calculations, simulation results for the machine with fixed and frequency-adaptive hysteresis coefficients were applied to a selected EV. The vehicle's accumulated iron energy loss was then evaluated for both methods. The deviation in accumulated iron energy loss between the two approaches is approximately 12% during the WLTC test drive cycle for the chosen EV. This indicates that using a fixed coefficient overestimates the accumulated energy loss in the vehicle by 12% compared to the proposed frequency-adaptive method.

Fig. 9 summarizes the steps defined to improve the core loss calculation.

B. THREE-PHASE INVERTER

As mentioned, recent versions of commercial-WBG SiC MOSFETs offer a compelling alternative to conventional Si-IGBTs in electrified vehicle applications. Their appeal stems from reduced switching losses due to faster transition times and superior thermal characteristics, making them preferable to Si-IGBTs. In addition, the MOSFET's reverse conduction (RC) phenomenon allows for lower conduction losses. A half-bridge SiC module, CAS300M17BM2 [20], has been utilized to implement the PWM-based motor drive inverter. The inverter is configured as a three-phase two-level VSI within the Twin Builder tools. To develop accurate loss models, the measured currents and instantaneous voltages obtained from the real-time cosimulation between Twin Builder and Ansys Maxwell have been imported into MATLAB for numerical loss model implementation, which is detailed in later subsections.

1) CONDUCTION LOSSES

The numerical implementation relies on an analytical approach for determining the losses in SiC MOSFETs, as outlined in [21] and [22]. In this method, the average MOSFETconduction losses over a fundamental period of the phase current can be calculated as

$$P_{\text{cond,MOS}} = \frac{1}{2\pi}\int_0^{2\pi} R_{\text{on}} {I_{\text{M}}}^2(\alpha)\tau(\alpha)d\alpha \tag{7}$$

where R_{on} is the MOSFET ON-state resistance, I_{M} is the MOSFET current, $\alpha = 2\pi ft$, f is the fundamental frequency and τ is the duty cycle which can be expressed as a function of α as

$$\tau(\alpha) = \frac{1}{2}(1 + m\sin\alpha) \tag{8}$$

where m is the modulation index [23]. Likewise, the diode conduction losses can be derived as

$$P_{\text{cond,D}} = \frac{1}{2\pi}\int_0^{2\pi} (R_{\text{d}} {I_{\text{D}}}^2(\alpha) + V_{\text{d}} I_{\text{D}}(\alpha))\tau(\alpha)d\alpha \tag{9}$$

where the voltage drop, V_{d}, and the ON-state resistance, R_{d}, can be obtained from the datasheet information of the forward characteristics of the diode. Finally, I_{D} is the diode current.

1) *MOSFETs' RC:* Unlike Si-IGBTs, where the total reverse current of the transistor flows through an anti-parallel diode, MOSFETs can also conduct reverse current due to their RC characteristic. Thus, if the MOSFET's drain-to-source voltage exceeds the corresponding diode forward voltage, parallel conduction of the two devices occurs. The diode may be either a separate diode

or the intrinsic built-in one. This leads to a significant reduction, especially in the total conduction losses of the diodes. The currents flowing through the MOSFET and diode during RC can be obtained as

$$I_{\mathrm{M}} = \frac{R_{\mathrm{d}} I_{\mathrm{p}} \sin(\alpha - \varphi) - V_{\mathrm{d}}}{R_{\mathrm{d}} + R_{\mathrm{on}}} \tag{10}$$

$$I_{\mathrm{D}} = \frac{R_{\mathrm{on}} I_{\mathrm{p}} \sin(\alpha - \varphi) + V_{\mathrm{d}}}{R_{\mathrm{d}} + R_{\mathrm{on}}} \tag{11}$$

where φ is the angle of displacement power factor and I_{p} is the peak phase current [21], [22].

2) *Blanking time:* To incorporate the impact of blanking time (during which both the upper and lower switches in the same phase leg are turned OFF, allowing only the diode to conduct) into the calculation of conduction power losses, an equivalent duty cycle can be introduced as follows. This equivalent duty cycle is subsequently used in the MOSFET conduction loss equations mentioned earlier

$$\tau_{\mathrm{eq}}(\alpha) = \tau(\alpha) - t_{\mathrm{blanking}} f_{\mathrm{sw}}$$
$$= \frac{1}{2}(1 - 2t_{\mathrm{blanking}} f_{\mathrm{sw}} + m \sin \alpha) \tag{12}$$

where f_{sw} is the switching frequency [21], [22].

2) SWITCHING LOSSES

During every turn-ON and OFF events, a loss occurs in the switch and its anti-parallel/ body diode. Switching losses can be calculated analytically in a MOSFET and a diode by the expression

$$P_{\mathrm{sw,MOSFET,Diode}} = f_{\mathrm{sw}} \cdot E_{\mathrm{sw(I_{nom}, V_{nom})}} \cdot \left(\frac{1}{\pi} \frac{I_{\mathrm{p}}}{I_{\mathrm{nom}}}\right)^{k_{\mathrm{i}}} \cdot \left(\frac{V_{\mathrm{dc}}}{V_{\mathrm{nom}}}\right)^{k_{\mathrm{v}}} \tag{13}$$

where E_{sw} is switching energy loss, I_{p} is the peak phase current, I_{nom} and V_{nom} are nominal current and voltage values, and k_{i} and k_{v} are current and voltage dependency exponents, respectively [24]. In the numerical implementation in this study, the switching loss is calculated at every switch-ON and switch-OFF event of the device as

$$P_{\mathrm{sw}} = \frac{\sum E_{\mathrm{sw}}}{t} \tag{14}$$

where t is the fundamental period time.

3) THERMAL MODEL

Since parameters in power modules, such as ON-state resistances, forward voltage drops, as well as switching and reverse recovery energies exhibit temperature dependence, inverter power losses are calculated using the thermal network shown in Fig. 10. T_{j}, represents the junction temperatures of the MOSFET, and diodes, T_{c} is the case/baseplate temperature, T_{s} and T_{f} represent the heatsink and fluid temperatures, respectively. The fluid temperature and fluid flow-rate are set to 65°C and 10 L/min, respectively.

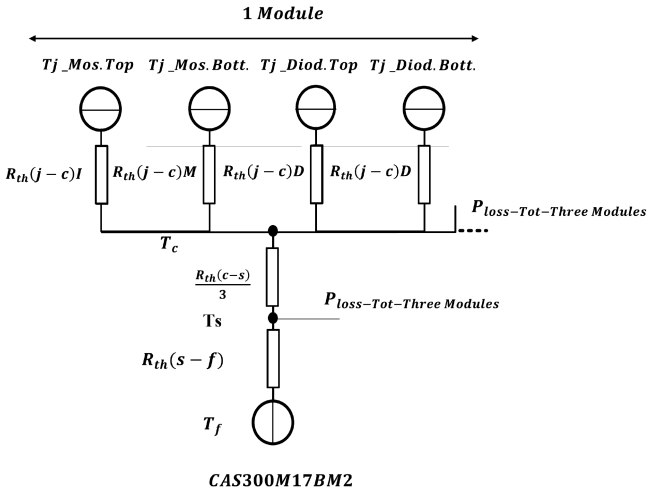

FIGURE 10. Thermal calculation model for SiC module in three-phase inverter.

The total losses are computed based on temperature using an iterative method. In this approach, the devices' static and dynamic parameters (V_{d}, R_{d}, R_{on}, E_{sw} and E_{rr}) are interpolated based on a specified junction temperature. Subsequently, the losses and temperatures are recalculated iteratively until convergence [21]. Notably, the current dependency of the devices' switching energies is also modeled as a function of current and junction temperature. Previous work by the authors has already provided a detailed examination of temperature's influence on both switching and conduction losses in SiC and IGBT modules [21], [25].

III. SYSTEM LEVEL POWER LOSS ANALYSIS WITH DIFFERENT PWM SWITCHING FREQUENCIES

As discussed previously, this study put the main focus on an optimized system-level loss analysis to address the optimum PWM frequency in all drive regions. The following section will provide the proposed PWM-induced power-loss analysis for the IPM as well as the SiC-based inverter for three selected operating points with the impact of different PWM frequencies. More broadly, the proposed scheme will be further extended to all feasible operating points within the torque–speed region of the studied machine to achieve the optimal switching frequency map through a drive system loss minimization approach.

A. PWM CURRENT RIPPLE ANALYSIS WITH DIFFERENT SWITCHING FREQUENCIES

The classical SVPWM modulation scheme, which is easily implemented, enables more efficient utilization of the dc-bus voltage (by 15%).

Applying the cosimulation process depicted in Figs. 1 and 2, the generated PWM-induced current ripples injected into the PMSM have been analyzed for two selected machine operating conditions: one heavy-load, low-speed, and one light-load, medium-speed scenario from the drive region. The

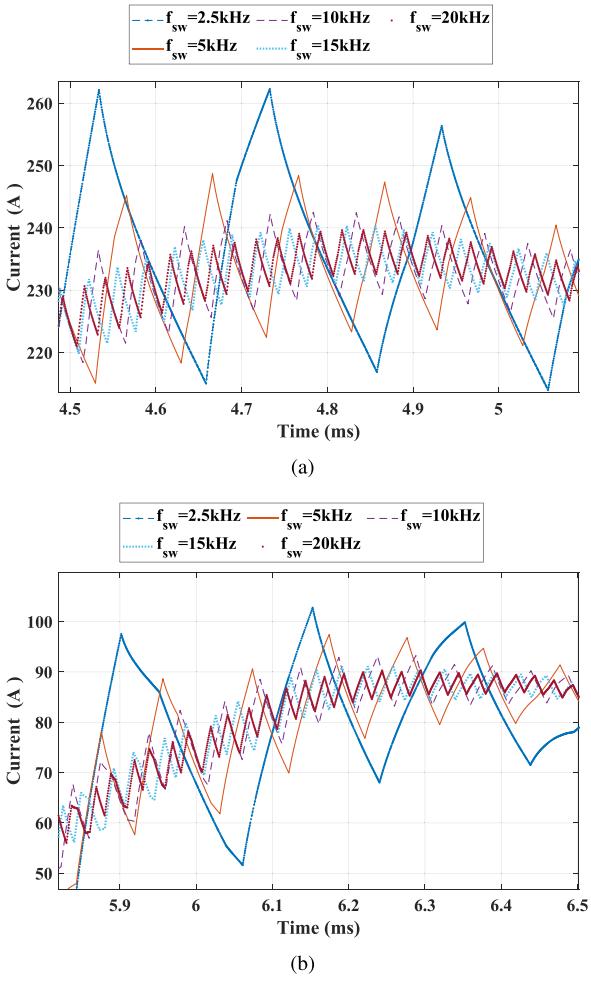

FIGURE 11. PWM-induced current ripples versus switching frequency for the PMSM, operating at heavy and light-load conditions at (a) 2000 r/min, 240 N · m and (b) 4000 r/min, 80 N · m.

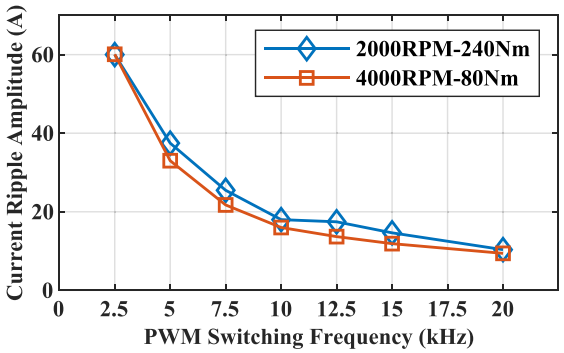

FIGURE 12. PWM-induced current ripple amplitude versus PWM switching frequencies for two selected machine conditions.

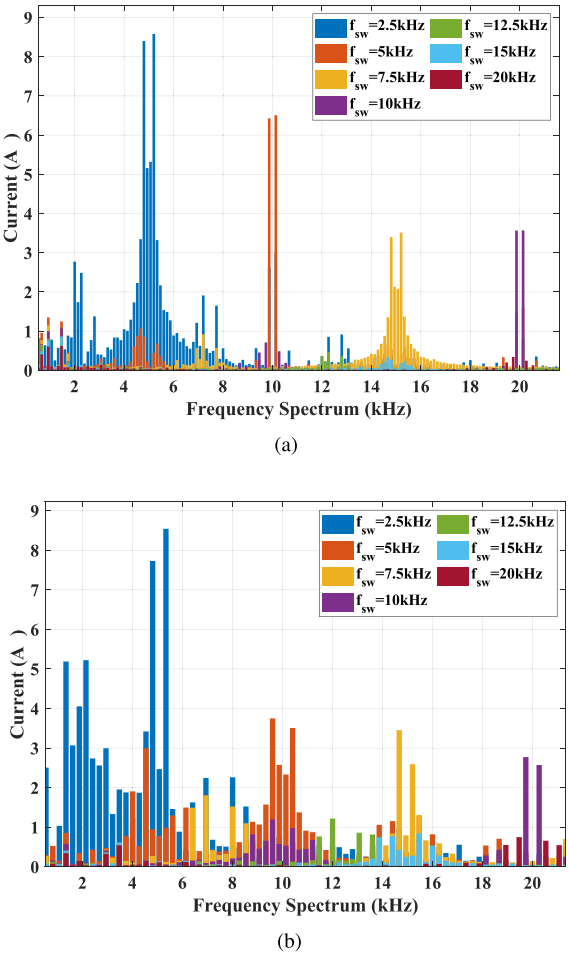

FIGURE 13. Fourier analysis of PWM-induced current ripples versus switching frequency for PMSM, operating at heavy and light-load conditions at (a) 2000 r/min, 240 N · m and (b) 4000 r/min, 80 N · m.

testing covered a range of PWM switching frequencies from 2.5 to 20 kHz.

Fig. 11 illustrates the PWM-induced current ripples versus switching frequency for the IPM used, operating at 2000 and 4000 r/min, generating electromagnetic torques of 240 and 80 N · m, respectively. The current ripple amplitude values are displayed in Fig. 12, showing that the ripple amplitudes for both conditions decrease monotonically as the PWM frequencies increase. However, the difference in ripple magnitude diminishes for PWM frequencies above 12.5 kHz.

Next, for a clearer comparison of their frequency components, the results of the Fourier analysis including the low frequency and switching frequency components are shown in Fig. 13.

As observed in both selected machine conditions, the dominant harmonics are concentrated around twice the PWM switching frequency. For instance, a switching frequency of 2.5 kHz results in a current ripple of 5 kHz. The values of the harmonic components decrease as the PWM switching frequency increases.

In fact, the higher the current ripple, the more significant the harmonic content in the current waveform. These harmonics generate corresponding harmonics in the magnetic flux density, which are superimposed on the fundamental flux component, leading to an overall increase in flux density

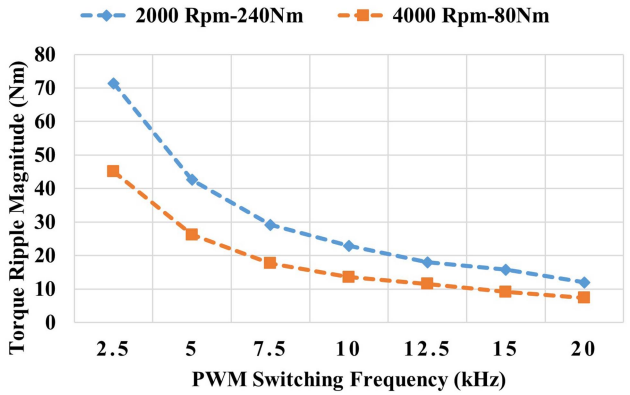

FIGURE 14. PWM-induced power losses in the machine versus PWM switching frequencies for three selected machine conditions.

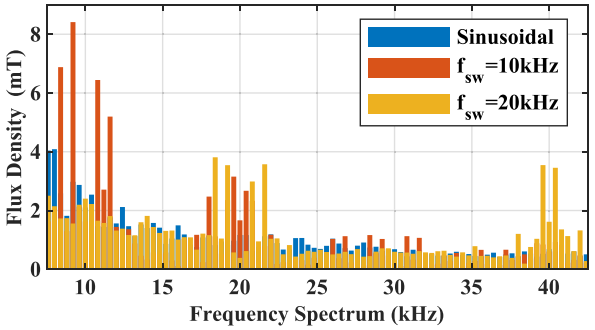

FIGURE 15. Frequency spectrum of the normal flux density of a mesh element on the middle of the stator tooth, at sinusoidal current feeding versus PWM-fed excitation with switching frequency of 10 and 20 kHz at the operating point of 60 N · m and 6000 r/min.

swings. Harmonics can also lead to torque ripple, causing mechanical vibrations and noise. Figure 14 illustrates the torque ripple magnitude at two selected operating points. As seen with the current ripple trends in Fig. 12, the torque ripple amplitude progressively decreases with increasing PWM frequency. However, beyond 12.5 kHz, the reduction in ripple magnitude becomes less significant.

Therefore, it is crucial to account for these harmonics, especially if the machine operates across a wide range of switching frequencies. Higher switching frequencies will push these harmonics out to higher frequencies, where they might have less impact on the machine's performance.

Based on the discussion above, this analysis underscores the importance of selecting an optimal switching frequency over the drive regions to minimize current ripple and improve the overall performance of the PMSM drive system.

B. PWM-INDUCED POWER LOSSES IN IPM

To calculate PWM-induced power losses in the IPM and assess the impact of PWM switching frequency, the losses are categorized into three components: copper losses, core losses, and magnet losses. As discussed in Section II-A1, the core losses, comprising both hysteresis and eddy current losses, are adjusted first, using a method that adapts the core loss coefficients to the frequencies of a specific operating point, providing an improved core loss calculation. To verify the impact of varying PWM switching frequencies on machine losses, an additional operating condition at 6000 r/min and 60 N · m torque was evaluated. Fig. 14 presents the PWM-induced losses in the machine across a wide range of PWM switching frequencies (5–30 kHz), calculated using real-time FEM cosimulation between Twin Builder and Ansys Maxwell with a variable time-step of up to 100 ns for three selected operating conditions. Furthermore, the conventional sinusoidal feeding excitation losses in the machine are compared with the PWM-induced losses, as illustrated in the figure.

As observed across the selected machine conditions, varying the switching frequency noticeably impacts magnet losses, with a decrease in magnet loss as the PWM frequency increases. However, the reduction in core and copper losses is minimal. This is because, at higher PWM switching frequencies, high-frequency harmonics become less effective in inducing eddy currents in the magnets, leading to lower magnet losses. In contrast, this effect is much less pronounced for core and copper losses, resulting in only a slight reduction.

As discussed before, core losses are primarily dependent on the fundamental frequency of the magnetic flux, which is related to the rotor speed. For the copper losses, although higher PWM frequencies can reduce current ripple, the impact on copper losses is relatively small because these losses are predominantly determined by the rms value of the current rather than the ripple. That is why those losses are less affected by changes in PWM frequency compared to magnet losses.

Comparing the sinusoidal excitation loss bars with PWM in Fig. 14, PWM excitation leads to significantly higher magnet losses due to increased eddy currents from switching harmonics. In contrast, sinusoidal excitation typically results in smoother loss behavior with fewer high-frequency components. Therefore, accounting for these additional losses is critical when designing high-efficiency systems utilizing PWM, particularly in high-speed or high-power applications.

As mentioned earlier, the overall core losses increase when the IPM is fed with an inverter instead of a sinusoidal voltage source. Moreover, by increasing the switching frequency the core losses are observed to be reduced. To investigate the impact of PWM on the core losses and verify that the proposed core loss calculation correctly accounts for PWM-induced losses, understanding the changes in flux density is crucial. To do so, an exemplary operating point with a torque of 60 N · m and speed of 6000 r/min is selected. Fig. 15 shows the frequency spectrum of the normal flux density for a mesh point in the middle of the stator tooth, shown in Fig. 6. For the sake of comparison, the frequency components of the normal flux density with sinusoidal feeding are compared to those of utilizing PWM-fed excitation at switching frequencies of 10 and 20 kHz.

As can be seen, by including the inverter's switching, frequency components on the sidebands of switching frequency's

multiples, increase. To verify that the model used for core losses with frequency-adaptive coefficient is correctly accounting for the effect of PWM, additional measurements on the electrical steel used in this study were performed at 10 and 20 kHz. At sinusoidal excitation, the core loss density of the selected mesh point is 26.3 W/kg. This value increases to 28.3 W/kg with a switching frequency of 10 kHz and a slightly lower value of 28.1 W/kg for a switching frequency of 20 kHz. The core loss increase due to switching events is 6% to 7% for this mesh point. However, the core loss increase on both the stator and rotor surfaces is approximately 22% for switching frequencies of 10 and 20 kHz at the selected operating point. This is because the frequency component of the flux density varies depending on the position of the mesh element on the stator and rotor core geometry.

C. PWM-INDUCED POWER LOSSES IN SIC-BASED INVERTER

As discussed in Section II-B, the CAS300M17BM2 half-bridge SiC module was used to configure a three-phase VSI inverter to drive the PMSM. To achieve a more precise inverter loss calculation, three-phase currents, and reference voltages at varying PWM switching frequencies were extracted from the real-time cosimulation and imported into MATLAB. A numerical analysis based on the MOSFETs/diodes' conduction and switching loss models [21], was conducted across all the machine operating points. The impact of thermal feedback and diode blanking time on the losses has been evaluated.

As an example, Fig. 16 shows the three-phase currents and the SVM reference voltages fed to the SiC-based inverter, along with the generated three-phase PWM-induced voltages at 2000 r/min and 380 N · m machine operating condition with a 10 kHz PWM switching frequency in the implemented real-time cosimulation. Following this, Fig. 17 illustrates the conduction losses for the upper MOSFET and its corresponding diode during parallel conduction [21], [22]. Furthermore, the diode conduction losses that occur during the blanking time are highlighted in Fig. 17(b).

To assess the impact of varying the PWM switching frequency, the loss analysis discussed has been applied to the three operating points mentioned earlier. Fig. 18 illustrates the distribution of these losses as the PWM switching frequency increases from 5 to 30 kHz.

As predicted, across all three investigated points, increasing the PWM switching frequency substantially increases the MOSFET switching losses, particularly under heavy-load conditions. In contrast, the impact on the MOSFET conduction losses is minimal[21], [22]. In addition, the diode conduction losses observed under the selected operating conditions are negligible, though they show a slight increase with higher switching frequencies. This increase is linked to more current flowing through the diodes as the junction temperature rises with elevated switching frequencies [25], [26]. Worth mentioning is that, from the datasheet, the diode switching energy for the employed SiC module is zero.

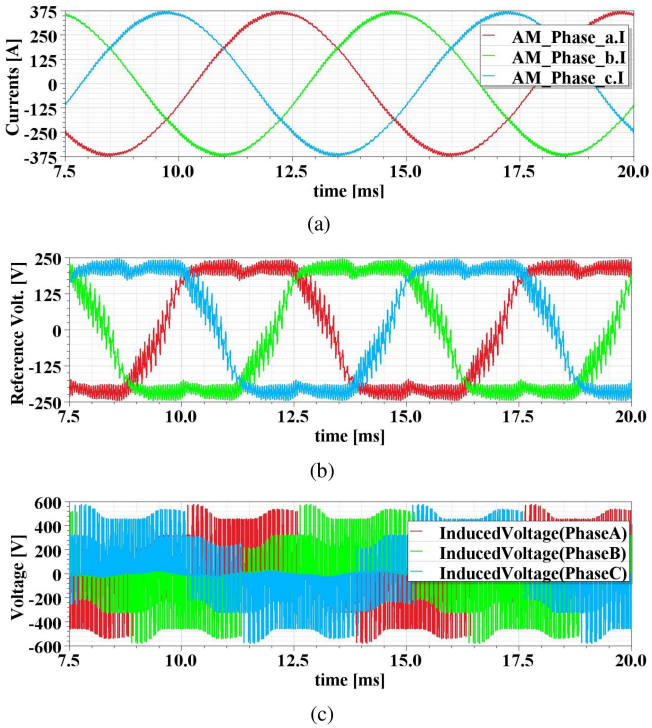

FIGURE 16. Three-phase input signals fed to SiC inverter as well as the generated three-phase PWM output at 2000 r/min, 380 N · m, 10 kHz switching frequency. (a) Three-phase currents. (b) SVM reference voltages. (c) PWM-induced voltages.

D. OPTIMUM SWITCHING FREQUENCY DETERMINATION

As the PWM switching frequency expands from 2.5 to above 50 kHz (65 kHz), the trend of total losses within the drive system, including both the PMSM and the SiC-based inverter, becomes more clearly evident across the two tested operating points, as shown in Fig. 19.

As illustrated in the figure, as the PWM switching frequency increases, the decline in PMSM losses gradually diminishes, while the inverter losses rise linearly. At a certain switching frequency, these opposing trends balance each other out, resulting in minimum total losses for the drive system. For the example operating points, these optimal frequencies are identified at 20 and 30 kHz, as shown by the red circles.

This approach has been utilized to determine the optimal switching frequency across all operating regions of the drive system, which will be evaluated in the following section.

IV. OPTIMAL PWM SWITCHING FREQUENCY SCHEME: OVERALL SIC MOTOR DRIVE SYSTEM

By applying the previously discussed loss calculation methods at various operating points in drive regions under different switching frequencies, the optimal switching frequency scheme can be visualized in the drive system's torque–speed map; see Fig. 20.

The optimal PWM switching frequencies assigned to each drive region will result in the lowest possible system (inverter and PMSM) losses.

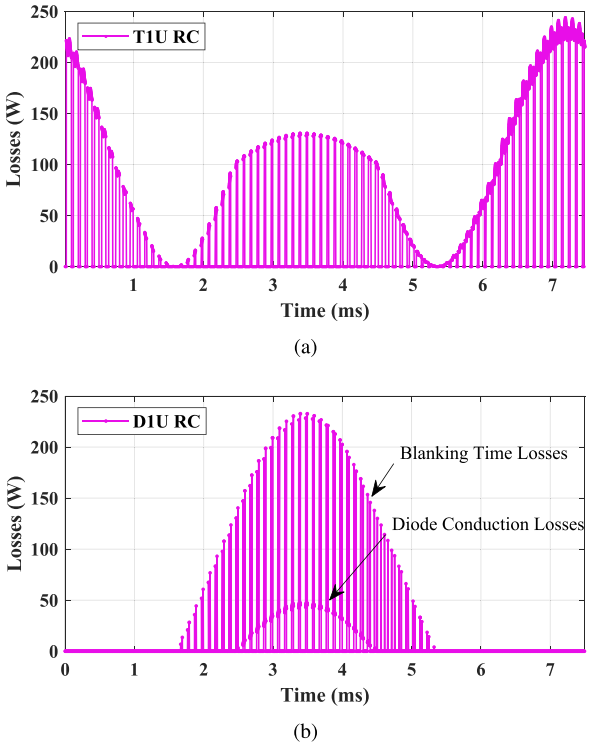

FIGURE 17. Parallel conduction losses of MOSFET and diode showing MOSFET RC phenomenon in a phase leg of SiC inverter at 2000 r/min speed, 380 N · m torque and 10 kHz switching frequency. (a) Upper MOSFET. (b) Upper corresponding diode.

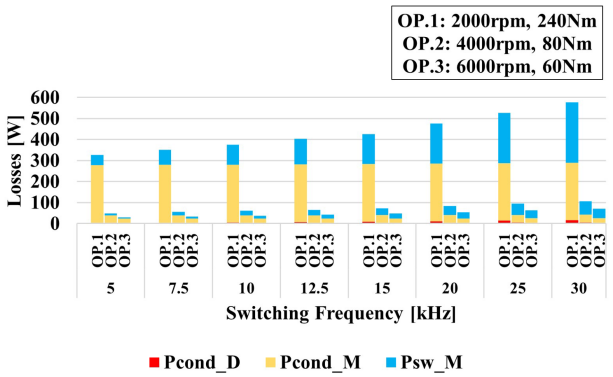

FIGURE 18. PWM-induced power losses in SiC-based inverter versus PWM switching frequencies for three selected machine conditions.

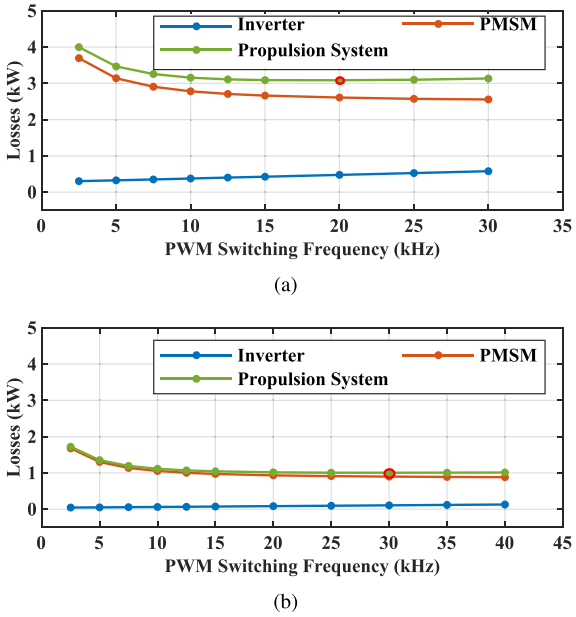

FIGURE 19. Optimum PWM switching frequency determination in a total system loss minimization approach for two selected machine conditions at (a) 2000 r/min, 240 N · m and (b) 4000 r/min, 80 N · m.

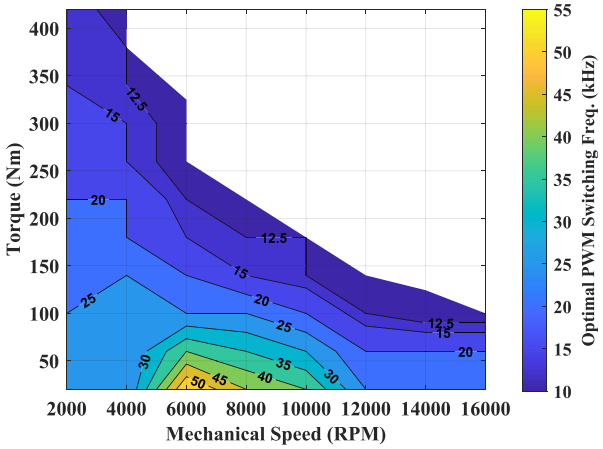

FIGURE 20. Optimal PWM switching frequency scheme of SiC-based motor drive system.

As can be observed, the optimal switching frequency is distributed in a pattern of concentric levels. As the value of the switching frequency decreases, it becomes associated with the outer layers of this pattern. In other words, higher frequencies are associated with the inner layers within the medium-speed range between 5000 and 10 000 r/min with low torque, and lower frequencies are found in the outer layers for high torque regions. In addition, in the high-speed region, the optimal switching frequency value gradually decreases as the speed increases.

This pattern can indicate how the optimal switching frequency varies with different drive conditions or operational parameters, potentially guiding the selection of switching frequencies to minimize the losses and improve the motor drive performance.

It should be noted that while SiC devices theoretically support much higher switching frequencies, the trade off between machine inverter losses and overall drive performance must be carefully evaluated. Excessively high frequencies can lead to increased inverter losses, high slew rate effects, and electromagnetic interference (EMI), ultimately compromising system efficiency. The detailed analysis in this study indicates that for automotive applications.particularly the investigated

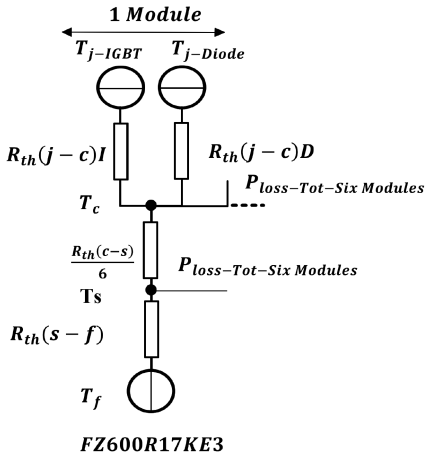

FIGURE 21. Thermal calculation model for Si-IGBT module in three-phase inverter.

drive system—operating beyond 50 kHz does not yield further efficiency benefits under realistic conditions.

A. OPTIMAL PWM SWITCHING FREQUENCY SCHEME: COMPARING SIC VERSUS IGBT-BASED INVERTERS IN MOTOR DRIVE SYSTEMS

To verify the advanced switching capabilities of SiC semiconductors compared to IGBTs, similar loss calculation methods including a speed-adaptive PMSM core loss calculation described in Section II-A1 and PWM-induced power losses into drive system (see Section III) were applied to a low-switching-loss Si-IGBT module with a blocking voltage of 1700 V, FZ600R17KE3 [27], using a Si-based inverter configuration for comparison.

For the inverter power loss calculations, the conduction losses of the Si-IGBT and diode in the Si-IGBT module have been calculated by integrating the product of the current flowing through the device and voltage drop over it [24], [28], resulting in the expressions

$$P_{\text{cond,IGBT}} = \frac{1}{2}\left(V_{\text{T}}\frac{I_{\text{p}}}{\pi} + R_{\text{f}}\frac{{I_{\text{p}}}^2}{4}\right) + \ldots \\ m\cos\varphi\left(V_{\text{T}}\frac{I_{\text{p}}}{8} + \frac{1}{3\pi}R_{\text{f}}{I_{\text{p}}}^2\right) \quad (15)$$

$$P_{\text{cond,Diode}} = \frac{1}{2}\left(V_{\text{d}}\frac{I_{\text{p}}}{\pi} + R_{\text{d}}\frac{{I_{\text{p}}}^2}{4}\right) - \ldots \\ m\cos\varphi\left(V_{\text{d}}\frac{I_{\text{p}}}{8} + \frac{1}{3\pi}R_{\text{d}}{I_{\text{p}}}^2\right) \quad (16)$$

where R_{f} is the IGBT ON-state resistance and V_{T} is the IGBT voltage drop.

The same analysis approach used for the SiC-based inverter was applied to calculate switching losses and diode conduction losses during the blanking time for the Si-IGBT inverter. In addition, the thermal model shown in Fig. 21, employing a similar calculation method as the SiC-based inverter, was utilized.

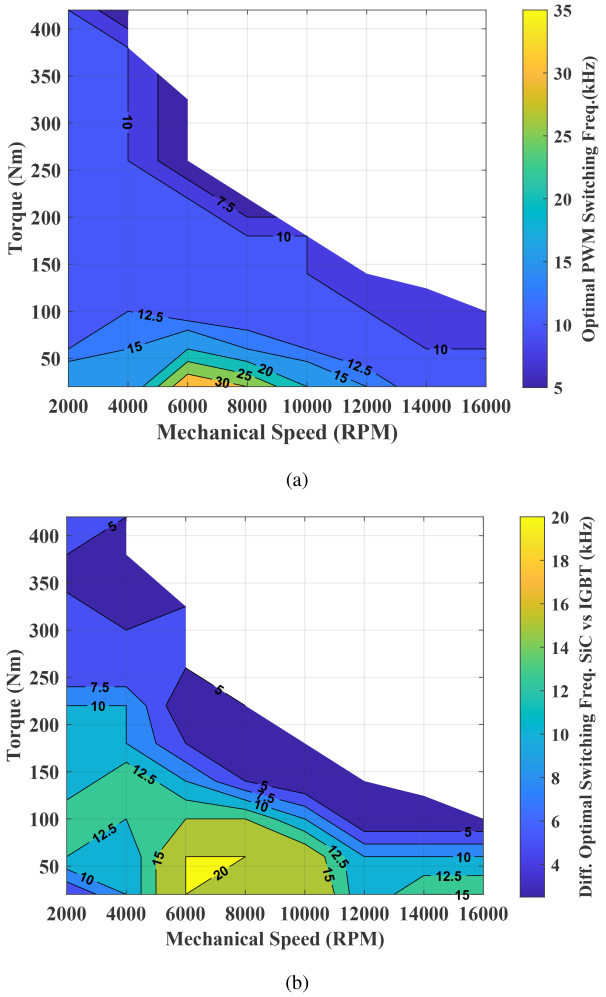

FIGURE 22. (a) Optimal PWM switching frequency scheme of IGBT-based motor drive system. (b) The difference in optimal switching frequency values between SiC-based and IGBT-based motor drives.

Following the approach used for the SiC-based drive system to determine the optimal switching frequency, the method was applied to identical operating points across the drive regions under different PWM switching frequencies.

Fig. 22 shows the distribution of the optimal switching frequency on the torque–speed map for the Si-IGBT-based drive system to achieve the minimum possible system losses, while Fig. 22(b) illustrates the difference in optimal switching frequency between the two motor drive systems.

As shown, in the IGBT drive system, the typical PWM switching frequency range is limited to 5 to 30 kHz. In contrast, the SiC-based drive system exhibits a broader PWM frequency distribution, i.e., 10–50 kHz due to its ability to operate at higher switching frequencies with lower switching losses compared to the Si-IGBT system. In addition, as shown in Fig. 22(b), the major difference, up to 20 kHz occurs in the low-speed to medium-speed ranges with low torque, where

TABLE 2. EV Parameters

Parameter	Abbreviation	Value	Unit
Aerodynamic drag coefficient	C_d	0.340	NA
Frontal area	A_f	2.300	m^2
Air density	ρ_a	1.2	kg/m^3
Rolling resistance coefficient	C_r	0.009	NA
Vehicle mass	m	1700	kg
Tire radius	r_t	0.28	m
Gear ratio	R_g	12.5	NA

EVs predominantly operate. In other drive regions in the figure, the optimal frequency difference between the two motor drive systems is still substantial.

The findings presented in the previous section show that, using the proposed loss map method, the SiC-based drive system can leverage the high switching frequency capability of SiC MOSFETs to optimize the PWM frequency across different regions of the drive system over a broader range compared to that of IGBTs, thereby enhancing the machine performance.

B. OPTIMAL PWM SWITCHING FREQUENCY SCHEME: DRIVE CYCLE AND ENERGY LOSS ANALYSIS, COMPARING SIC VERUS IGBT-BASED INVERTERS IN MOTOR DRIVE SYSTEMS

In this section, the EM under study is integrated into the powertrain of a medium-sized battery EV, which is operated under the WLTC test-drive cycle to analyze the predicted accumulated energy loss. Three case studies are investigated. In Case A, the EM is sinusoidally fed in an FEM simulation with an inverter operating at a fixed switching frequency of 10 kHz. Case B examines a PWM-fed machine driven by an inverter with a fixed 10 kHz switching frequency in a coupled FEM simulation of the PMSM and inverter. Case C implements the proposed method in the current study, using a variable PWM-fed machine in the coupled FEM analysis. These studies were conducted for both a SiC-based inverter and an IGBT counterpart.

The vehicle dynamics and forces on the vehicle can be described, according to [29], as

$$F_{\text{wheel}} = \frac{\rho_a}{2} C_d A_f v^2 + C_r mg\cos\alpha + mg\sin\alpha + m\frac{dv}{dt} \quad (17)$$

where ρ_a represents the air density, C_d is the aerodynamic drag coefficient. m is the vehicle mass, g is the gravitational constant, α is the road inclination angle, and C_r is the dimensionless rolling resistance coefficient. The parameter A_f is the effective cross sectional area. The power required by the wheels to sustain a certain speed is then obtained by $P_{\text{wheel}} = F_{\text{wheel}}(t)v_{\text{car}}(t)$. The total accumulated energy consumed at the wheels is determined as

$$E_{\text{wheel}}(t) = \int P_{\text{wheel}}(t)dt. \quad (18)$$

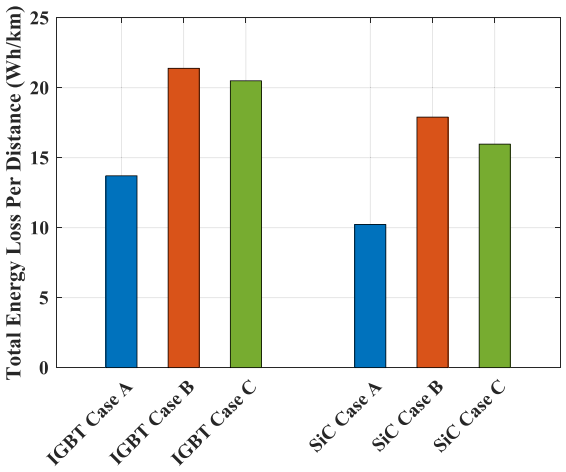

FIGURE 23. Total energy loss per distance in a selected EV in WLTC test drive cycle.

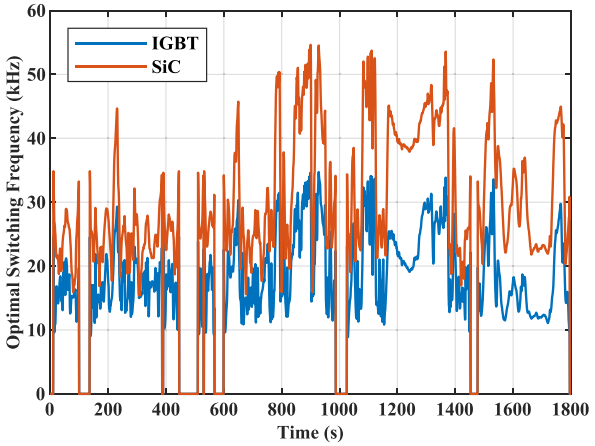

FIGURE 24. Optimal PWM switching frequency for IGBT and SiC switches under driving conditions of WLTC test-drive cycle.

The dynamic parameters of the vehicle are presented in Table 2 and Fig. 23 shows the results of vehicle assessment in the WLTC drive cycle.

As shown, in all three cases, the SiC-based drive consistently minimizes energy losses compared to the IGBT-based system. The sinusoidal current excitation of the machine (Case A) for both SiC and IGBT drives notably underestimates power and energy losses in the system. Looking at the bar charts for Cases B and C (IGBT and SiC), the proposed optimal PWM frequency profile (Case C) results in a 10.78% reduction in accumulated energy loss for the SiC-based inverter and a 4.17% reduction for the IGBT-based inverter compared to the fixed PWM frequency (Case B). In addition, implementing the proposed method (Case C) leads to 22 % lower energy losses in the SiC-based drive compared to the IGBT counterpart, as the optimal PWM switching frequency pattern over the WLTC cycle is illustrated in Fig. 24. It can be seen that the major difference, reaching up to 20 kHz,

in the optimal frequency patterns occurs in the low-speed to medium-speed ranges over the WLTC, as also observed in the previous section.

V. CONCLUSION

This article determines the optimal system-level switching frequency throughout the torque–speed map. The work can be summarized in the following points.

1) Of the main components of machine losses, PWM-induced iron loss is identified as the dominant factor, influenced by speed/fundamental frequency. To provide a more reliable measure of PMSM losses, a method is used to adapt iron loss coefficients across different frequencies/speeds based on measurements on the electro-steel sheets. This approach differs from the conventional method of using a fixed iron loss coefficient over the operating region, especially in high-frequency/high-speed PWM-based applications. The results reveal that the calculated losses from fixed coefficient by using all the datasets from the measurements mainly overestimate the core losses at most frequencies of up to 80% and approximately 12% in the WLTC test drive cycle for the selected EV.
2) A detailed real-time coupled simulation of Twinbuilder and Ansys Maxwell FEM analysis of PWM-induced power losses in IPM machines has been implemented. Enabled by a WBG-based VSI, leveraging its advanced switching capabilities, the analysis spans a wide range of PWM switching frequencies from 5 to 50 kHz (65 kHz). A numerical inverter loss model is employed in MATLAB, accounting for thermal feedback, blanking time, and MOSFET RC, driven by the generated three-phase PWM currents and voltages from the real-time coupled FEM simulation, to provide an accurate estimate of inverter side losses.

This comprehensive approach makes it possible to capture the complex dynamics between the motor and the inverter, and then the developed powertrain loss map models offer a more reliable method to determine the optimal switching frequency throughout the full operating range of the machine.

For the intended scope of this analysis, the results indicate that increasing the PWM switching frequency has promising potential for minimizing PWM-induced power losses in IPM machines, reducing all three major loss components: core losses, copper losses, and magnet losses, with a notable reduction in magnet losses. Although system-level efficiency is closely related to inverter-side losses—particularly switching losses, which increase with switching frequency—the optimal switching frequency offered by the SiC-based inverter shows a broad range of 10–50 kHz over the torque-speed map and a difference of up to 20 kHz in the dominant driving range of light load and medium speed compared to the IGBT-based motor drive. This is due to significantly higher switching losses from adopting a higher PWM frequency, which constrains the optimal PWM frequency to a lower range in IGBT-based counterparts.

Furthermore, the optimal PWM frequency profile generated in this study presents a reduction of up to 22% on the accumulated energy loss over the WLTC driving pattern in the SiC motor drive compared to the IGBT counterpart. In addition, a decline of 10.78% in energy loss has been achieved for the SiC drive system and 4.17 % for the IGBT counterpart using the proposed optimal PWM frequency profile compared to using a fixed switching frequency.

For future work, this study can be expanded to consider the effect of high switching speed (high slew rate *dv/dt*) in WBG-based motor drives on inverter losses, providing a tradeoff between the turn-OFF voltage overshoot caused by a high *dv/dt* and the resulting switching losses, as well as the effect of electromagnetic interference and mechanical losses in the system. In addition, since inverter and machine losses likely exhibit different behaviors with varying dc-bus voltages, the effect of variable dc-link voltages on both IPM and inverter loss calculations can be evaluated. Moreover, to predict the core losses of the EM precisely, the effect of manufacturing of EMs on the electro-steel can be taken into account. Considering the abovementioned factors allows for a more accurate estimation of system-level losses, leading to a more reasonable determination of the optimal switching frequency scheme for the electric drive system. However, emphasizing experimental validation is equally crucial. While experimental setups may not cover a full range of parameters or conditions required for a complete comparison with the FEM results, they can certainly complement the findings.

VI. DECLARATION OF COMPETING INTEREST

The authors declare that they have no known competing financial interests or personal relationships that could have appeared to influence the work reported in this article.

REFERENCES

[1] A. Y. Saber and G. K. Venayagamoorthy, "Plug-in vehicles and renewable energy sources for cost and emission reductions," *IEEE Trans. Ind. Electron.*, vol. 58, no. 4, pp. 1229–1238, Apr. 2011, doi: 10.1109/TIE.2010.2047828.

[2] C. C. Chan, A. Bouscayrol, and K. Chen, "Electric, hybrid, and fuel-cell vehicles: Architectures and modeling," *IEEE Trans. Veh. Technol.*, vol. 59, no. 2, pp. 589–598, Feb. 2010, doi: 10.1109/TVT.2009.2033605.

[3] J. O. Estima and A. J. M. Cardoso, "Efficiency analysis of drive train topologies applied to electric/hybrid vehicles," *IEEE Trans. Veh. Technol.*, vol. 61, no. 3, pp. 1021–1031, Mar. 2012, doi: 10.1109/TVT.2012.2186993.

[4] F. Yang, A. R. Taylor, H. Bai, B. Cheng, and A. A. Khan, "Using D–Q transformation to vary the switching frequency for interior permanent magnet synchronous motor drive systems," *IEEE Trans. Transport. Electrific.*, vol. 1, no. 3, pp. 277–286, Oct. 2015, doi: 10.1109/TTE.2015.2443788.

[5] Q. Li, D. Jiang, Y. Zhang, and Z. Liu, "The impact of VSF-PWM on dq current control and a compensation method," *IEEE Trans. Power Electron.*, vol. 36, no. 3, pp. 3563–3572, Mar. 2021, doi: 10.1109/TPEL.2020.3017776.

[6] O. Oñederra, I. Kortabarria, I. M. de Alegría, J. Andreu, and J. I. Gárate, "Three-phase VSI optimal switching loss reduction using variable switching frequency," *IEEE Trans. Power Electron.*, vol. 32, no. 8, pp. 6570–6576, Aug. 2017, doi: 10.1109/TPEL.2016.2616583.

[7] S. Yunus, W. Ming, and C. E. Ugalde-Loo, "Adaptive variable switching frequency control for SiC-based PMSM drive systems," in *Proc. IECON 2022–IEEE 48th Annu. Conf. Ind. Electron. Soc.*, 2022, pp. 1–6, doi: 10.1109/IECON49645.2022.9969050.
[8] S. Yunus, W. Ming, and C. E. UgaldeLoo, "Efficiency improvement analysis of a SiC MOSFET-based PMSM drive system with variable switching frequency," in *Proc. 23rd Eur. Conf. Power Electron. Appl.*, 2021, pp. 1–9, doi: 10.23919/EPE21ECCEEurope50061.2021.9570535.
[9] Y. Nakayama et al., "Efficiency improvement of motor drive system by using a GAN three phase inverter," in *Proc. 2019 IEEE Int. Conf. Ind. Technol.*, 2019, pp. 1599–1604, doi: 10.1109/ICIT.2019.8755018.
[10] S. Hori, "Application of variable carrier frequency control by using wide bandgap semiconductors inverter for WLTC mode driving," in *Proc. IEEE 22nd Int. Conf. Ind. Technol.*, 2021, vol. 1, pp. 322–326, doi: 10.1109/ICIT46573.2021.9453618.
[11] L. Chang, M. Alvi, W. Lee, J. Kim, and T. M. Jahns, "Efficiency optimization of PWM-induced power losses in traction drive systems with IPM machines using wide bandgap-based inverters," *IEEE Trans. Ind. Appl.*, vol. 58, no. 5, pp. 5635–5649, Sep./Oct. 2022, doi: 10.1109/TIA.2022.3178979.
[12] L. Chang, W. Lee, T. M. Jahns, and K. Rahman, "Investigation and prediction of high-frequency iron loss in lamination steels driven by voltage-source inverters using wide-bandgap switches," *IEEE Trans. Ind. Appl.*, vol. 57, no. 4, pp. 3607–3618, Jul./Aug. 2021, doi: 10.1109/TIA.2021.3075647.
[13] D. Ionel, M. Popescu, S. Dellinger, T. Miller, M. McGilp, and R. Heideman, "Factors affecting the accurate prediction of iron losses in electrical machines," in *Proc. IEEE Int. Conf. Electric Mach. Drives*, 2005, pp. 1625–1632, doi: 10.1109/IEMDC.2005.195937.
[14] A. Krings and J. Soulard, "Overview and comparison of iron loss models for electrical machines," *J. Elect. Eng.*, vol. 10, pp. 162–169, May 2010.
[15] S. Soltanipour, T. Thiringer, and J. Lindström, "Battery electric vehicle performance evaluation by considering punching effect on pmsm iron cores," in *Proc. 2022 Int. Conf. Elect. Mach.*, 2022, 2022, doi: 10.1109/ICEM51905.2022.9910633.
[16] K. Bourchas, "Quantifying effects of cutting and welding on magnetic properties of electrical steels," *IEEE Trans. Ind. Appl.*, vol. 53, no. 5, pp. 4269–4278, Sep./Oct. 2017, doi: 10.1109/TIA.2017.2698400.
[17] A. Krings, "Iron losses in electrical machines —influence of material properties, manufacturing processes, and inverter operation," Ph.D. dissertation, KunglTekniskahögskolan, Stockholm, Sweden, 2014.
[18] IEC60404-2, "Methods of measurement of the magnetic properties of electrical steel strip and sheet by means of an epstein frame," Int. Electrotechnical Commission (IEC), 2008.
[19] D. Lin, P. Zhou, W. Fu, Z. Badics, and Z. Cendes, "A dynamic core loss model for soft ferromagnetic and power ferrite materials in transient finite element analysis," *IEEE Trans. Magn.*, vol. 40, no. 2, pp. 1318–1321, Mar. 2004, doi: 10.1109/TMAG.2004.825025.
[20] W. P. CAS300M17BM2. [Online]. Available: https://assets.wolfspeed.com/uploads/2024/01/Wolfspeed-CAS300M17BM2-data-sheet.pdf
[21] S. Amirpour, T. Thiringer, and D. Hagstedt, "Power loss analysis in a SiC/IGBT propulsion inverter including blanking time, MOSFET's reverse conduction and the effect of thermal feedback using a PMSM model," in *Proc. IECON 2020 IEEE 46th Annu. Conf. Ind. Electron. Soc.*, 2020, pp. 1424–1430, doi: 10.1109/IECON43393.2020.9254297.
[22] A. Acquaviva and T. Thiringer, "Energy efficiency of a SiC MOSFET propulsion inverter accounting for the MOSFET's reverse conduction and the blanking time," in *Proc. 19th Eur. Conf. Power Electron. Appl.*, 2017, pp. P.1–P.9, doi: 10.23919/EPE17ECCEEurope.2017.8099052.
[23] J. Kolar, H. Ertl, and F. Zach, "Influence of the modulation method on the conduction and switching losses of a PWM converter system," in *Proc. Conf. Rec. 1990 IEEE Ind. Appl. Soc. Annu. Meeting*, 1990, pp. 502–512, doi: 10.1109/IAS.1990.152232.
[24] SEMIKRON, *Application Manual Power Semiconductors*, Ilmenau, Germany: ISLE Verlag, 2015, pp. 274–279.
[25] S. Amirpour, T. Thiringer, and D. Hagstedt, "Energy loss analysis in a SiC/IGBT propulsion inverter over drive cycles considering blanking time, MOSFET's reverse conduction and the effect of thermal feedback," in *Proc. 2020 IEEE Energy Convers. Congr. Expo.*, 2020, pp. 1505–1511, doi: 10.1109/ECCE44975.2020.9236168.
[26] J. Rbkowski and T. Płatek, "Comparison of the power losses in 1700v Si IGBT and SiC MOSFET modules including reverse conduction," in *Proc. 17th Eur. Conf. Power Electron. Appl.*, 2015, pp. 1–10, doi: 10.1109/EPE.2015.7309444.
[27] I. P. FZ600R17KE3. (n.d.). [Online]. Available: https://www.infineon.com/dgdl/Infineon-FZ600R17KE3-DS-v03-00-EN.pdf?fileId=db3a304412b407950112b43044fb4fda
[28] F. Casanellas, "Losses in PWM inverters using IGBTs," *IEE Proc. - Electric Power Appl.*, vol. 141, no. 5, pp. 235–239, 1994.
[29] E. Grunditz, "BEV powertrain component sizing with respect to performance, energy consumption and driving patterns," Ph.D. dissertation, Dept. Energy Environ., Chalmers Univ. Technol., Göteborg, Sweden, Jun. 2014.

SEPIDEH AMIRPOUR received the B.Sc. degree in electrical engineering from the University of Guilan, Rasht, Iran, in 2004 and the M.Sc. degree in electrical engineering from the Kempten University of Applied Sciences, Germany, in 2013. She is currently working toward the joint Industrial Ph.D. degree with the Chalmers University of Technology, Gothenburg, Sweden, and ZEEKR, Gothenburg, working on refining the electric powertrains' efficiency.

Since 2016, she has been working as an Electric Drive Specialist with the Department of Vehicle Electronics and Software, ZEEKR Technology Europe, Gothenburg. Her research interests include power electronics in automotive and telecommunication applications, SiC/Si-based converter applications, electrical machines, and motor drive topologies focusing on power and energy loss modeling and optimization, thermal modeling, and reliability in the electric/hybrid powertrain.

SIMA SOLTANIPOUR (Member, IEEE) received the B.Sc. degree in electrical engineering from Arak University, Arak, Iran, in 2014, and the M.Sc. (Eng.) in electrical engineering from the Chalmers University of Technology, Gothenburg, Sweden, in 2020. She is currently working toward a joint Ph.D. degree with the Chalmers University of Technology and Volvo Cars Corporation, Gothenburg, whit a focus on electric machine design and efficiency improvement.

She joined Volvo Cars Corporation, as an industrial doctoral student, in 2021.

TORBJÖRN THIRINGER (Senior Member, IEEE) received the M.Sc. and Ph.D. degrees in electrical engineering from the Chalmers University of Technology, Gothenburg, Sweden, in 1989 and 1996, respectively.

He works as a Professor in applied power electronics with the Chalmers University of Technology. His research interests include the modeling, control, and grid integration of wind energy converters into power grids as well as power electronics and drives, e.g., for electrified vehicles, buildings, and industrial applications.

PRANAV KATTA received the M.S. degree in mobility engineering from the Chalmers University of Technology, Gothenburg, Sweden, in 2023.

He works with Volvo Cars Corporation, Gothenburg, as a Test Object Engineer within the Connected Experience Department. His research interests include electric propulsion, motor drives, and powertrain efficiency.